3D high spectral and spatial resolution imaging of *ex vivo* mouse brain

Sean Foxley[a)]
Department of Radiology, University of Chicago, Chicago, Illinois 60637

Miriam Domowicz
Department of Pediatrics, University of Chicago, Chicago, Illinois 60637

Gregory S. Karczmar
Department of Radiology, University of Chicago, Chicago, Illinois 60637

Nancy Schwartz
Department of Pediatrics, Department of Biochemistry and Molecular Biology, University of Chicago, Chicago, Illinois 60637

(Received 27 February 2014; revised 23 January 2015; accepted for publication 27 January 2015; published 2 March 2015)

Purpose: Widely used MRI methods show brain morphology both *in vivo* and *ex vivo* at very high resolution. Many of these methods (e.g., T_2^*-weighted imaging, phase-sensitive imaging, or susceptibility-weighted imaging) are sensitive to local magnetic susceptibility gradients produced by subtle variations in tissue composition. However, the spectral resolution of commonly used methods is limited to maintain reasonable run-time combined with very high spatial resolution. Here, the authors report on data acquisition at increased spectral resolution, with 3-dimensional high spectral and spatial resolution MRI, in order to analyze subtle variations in water proton resonance frequency and lineshape that reflect local anatomy. The resulting information compliments previous studies based on T_2^* and resonance frequency.

Methods: The proton free induction decay was sampled at high resolution and Fourier transformed to produce a high-resolution water spectrum for each image voxel in a 3D volume. Data were acquired using a multigradient echo pulse sequence (i.e., echo-planar spectroscopic imaging) with a spatial resolution of $50\times50\times70\ \mu m^3$ and spectral resolution of 3.5 Hz. Data were analyzed in the spectral domain, and images were produced from the various Fourier components of the water resonance. This allowed precise measurement of local variations in water resonance frequency and lineshape, at the expense of significantly increased run time (16–24 h).

Results: High contrast T_2^*-weighted images were produced from the peak of the water resonance (peak height image), revealing a high degree of anatomical detail, specifically in the hippocampus and cerebellum. In images produced from Fourier components of the water resonance at −7.0 Hz from the peak, the contrast between deep white matter tracts and the surrounding tissue is the reverse of the contrast in water peak height images. This indicates the presence of a shoulder in the water resonance that is not present at +7.0 Hz and may be specific to white matter anatomy. Moreover, a frequency shift of 6.76 ± 0.55 Hz was measured between the molecular and granular layers of the cerebellum. This shift is demonstrated in corresponding spectra; water peaks from voxels in the molecular and granular layers are consistently 2 bins apart (7.0 Hz, as dictated by the spectral resolution) from one another.

Conclusions: High spectral and spatial resolution MR imaging has the potential to accurately measure the changes in the water resonance in small voxels. This information can guide optimization and interpretation of more commonly used, more rapid imaging methods that depend on image contrast produced by local susceptibility gradients. In addition, with improved sampling methods, high spectral and spatial resolution data could be acquired in reasonable run times, and used for *in vivo* scans to increase sensitivity to variations in local susceptibility. [http://dx.doi.org/10.1118/1.4908203]

Key words: high spectral and spatial resolution imaging, mouse brain, MRI, microstructure, magnetic susceptibility

1. INTRODUCTION

Three-dimensional magnetic resonance imaging generates high contrast images of mouse brain with high spatial resolution.[1–6] The 3D anatomic detail, accuracy, and time efficiency of MRI make it an ideal modality for segmentation, quantification, and investigation of anatomic changes in murine brain due to gene mutations or genetic engineering.[7]

MRI methods used for high resolution imaging of mouse brain anatomy often depend on contrast produced by

variations in local magnetic susceptibility, and the resulting changes in resonance frequency. The magnetic susceptibility of tissue depends on the composition and arrangement of proteins, lipids, and (nonheme) iron in the tissue,[8,9] and thus is very sensitive to transitions between anatomic structures and tissues. T_2^*-weighted imaging is very sensitive to changes in the local magnetic field and thus is a powerful tool for studying normal and pathological tissue[10–13] allowing definition of distinct anatomic areas within the mouse brain. Extensions of T_2^*-weighting, often referred to as "phase sensitive" imaging or "susceptibility-weighted imaging," have further increased sensitivity to local susceptibility gradients, thereby providing exceptional anatomic detail.[14–21] Such methods are often used for both *in vivo* and *ex vivo* imaging.

While the T_2^* and phase sensitive/susceptibility-weighted imaging methods are very effective, they typically have low spectral resolution, and this reduces the accuracy of measurements of the local resonance frequency. As a result, conventional single echo acquisition techniques have limited sensitivity to the subtle variations in magnetic susceptibility due to microstructure predicted by white matter MRI signal models. These models predict small (on the order of Hz) but distinct changes in resonance frequency associated with white matter anatomy.[22–24]

In addition, sensitivity to non-Lorentzian features of the water resonance is limited because the apparent phase within a voxel detected by single echo methods is an average value over all frequency components of the measured signal. This is a necessary trade-off between spectral resolution, spatial resolution, and the volume of tissue that can be imaged with acceptable run-times.

The primary goal of the experiments described here was to compliment previous T_2^*-weighted, phase-sensitive, and susceptibility-weighted imaging studies by measuring local frequency shifts and water resonance lineshape with high precision. High-resolution proton spectra associated with each image voxel in a 3D volume were acquired using a multigradient echo pulse sequence (echo-planar spectroscopic imaging, EPSI).[25,26] This is consistent with the approach of multiple groups;[23,27] these researchers analyzed multigradient echo data in the temporal domain (i.e., the free induction decay or FID). Their results suggest subtle resonance frequency variations due to microstructural compartmentalization. Data in the present work were analyzed in the spectral domain to produce images based on the water resonance frequency and peak-height. This approach provides accurate measurements of the water (and fat) proton resonance frequency and spectral line shape in small voxels. In addition, the water peak-height images provide very strong T_2^* contrast without the diminished SNR and the artifacts associated with gradient echo imaging at long echo times. This approach has previously been reported to improve imaging of the breast[28–30] and prostate,[31–33] and fMRI applications have also been investigated.[34]

A second goal of this research was to evaluate images produced from the various Fourier components of the water resonance (FCIs) in each voxel. Data from this and other laboratories[35–37] suggest that different Fourier components of the water resonance represent distinct environments within each voxel, and can show distinct anatomical features.

2. METHODS

2.A. Preparation

All procedures performed on animals followed protocols approved by the Institutional Animal Care and Use Committee and were in compliance with the Animal Welfare Act and the NIH Guide for the Care and Use of Laboratory Animals. Adult mice ($n = 6$) were deeply anesthetized with 60 mg/kg pentobarbital and sacrificed by intercardial perfusion with 0.01M phosphate buffer saline solution (PBS), followed by 4% paraformaldehyde (pH 7.4)/PBS fixative solution. Brains were carefully removed from the skulls and postfixed in the same fixative overnight at 4 °C. Brains were washed in PBS prior to imaging for at least 2 h to remove fixative. MRI experiments were also performed using nonperfused archived brains with similar results.

2.B. MR imaging

Resected mouse brains were placed in 2 ml cryovials filled with fomblin (Ausimont, Thorofare, NJ). Fomblin, a perfluorinated polyether, serves as an ideal susceptibility-matching medium, minimizing artifacts at the brain surface due to magnetic susceptibility changes while yielding no proton signal.

Imaging was performed using a 20 cm internal diameter, horizontal bore Bruker BioSpec 9.4 T Small Animal MR System (Bruker Biospin, Billerica, MA) with a maximum gradient strength of 300 mT/m. Data were collected with the sample centered and securely fixed inside a quadrature volume coil (Bruker Biospin, Billerica, MA, OD/ID = 59/35 mm). Great care was taken to ensure that the positioning/orientation of the brain in the cryovial and the coil was consistent between experiments. This minimized variations in the water spectra due to orientation-dependent magnetic susceptibility.

Successive axial and coronal multislice gradient echo scans were performed to ensure proper, symmetric orientation of the subsequent 3D scan [fast low angle shot (FLASH), TR/TE = 500/5.5 ms, field of view (FOV) = 12.8 mm^2, in-plane resolution = 0.1 mm, slice thickness = 0.5 mm, number of excitations (NEX) = 2, and flip angle = 30°]. Fastmap[38] was performed on a cubic voxel (defined to encompass the entire brain but not extend beyond the fomblin into the fomblin/cryovial interface) to greatly improve localized shimming to the second order. The protocol was iteratively implemented until the linewidth across the whole brain volume was less than 10 Hz.

3D high spectral and spatial resolution (HiSS) data were acquired using EPSI (Fig. 1) to sample the entire free induction decay for each voxel (TR = 1000 ms, TE of first echo = 5.32 ms, subsequent echo spacing = 9.01 ms, number of echoes = 32, sampling duration = 284.63 ms, spectral resolution ~3.5 Hz, receiver band width = 50 kHz, flip angle = 45°, in-plane resolution = 0.05 mm, slice thickness = 0.07 mm, number of averages = 3, scan duration = 16–24 h, depending on the number of phase encoding steps required to cover the entire brain). 3D EPSI datasets were acquired with either coronal or sagittal orientations. Note that "3D" in the context of HiSS datasets

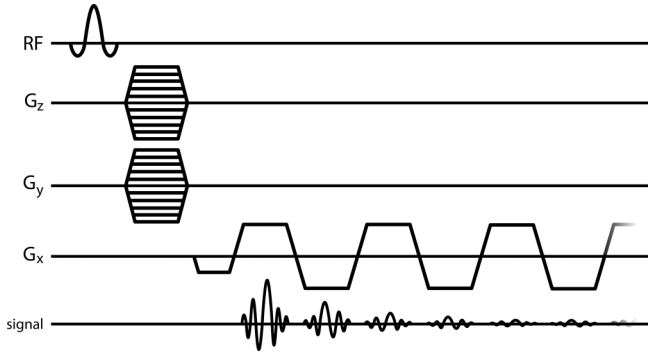

FIG. 1. 3D-EPSI pulse sequence.

indicates that data were acquired with three spatial dimensions (i.e., with the inclusion of a second phase encoding step). These datasets are, in fact, 4D, including time (t) along the free induction decay.

The T_2^* averaged over all voxels was 48.7 ± 5.8 ms (determined from voxel-by-voxel monoexponential fits). This is longer than reported values of T_2^* at 9.4 T in postmortem human brain tissue, which ranged between 20 and 30 ms;[39] however, murine brain is less iron rich than human.[40] Moreover, further effects may be due to the complex effects of fixation and subsequent soaking in PBS.[41]

Phantom studies using the same EPSI pulse sequence, but with a higher duty cycle than the present study, did not indicate a change in temperature due to the acquisition protocol;[42] therefore, temperature was not monitored during imaging of mouse brains.

2.C. Data processing

3D-HiSS datasets were processed using IDL 6.3 (ITT Visual Information Solutions, Boulder CO). Each 4D complex array ($k_x \times k_y \times k_z \times t$) was Fourier transformed in all dimensions to produce three spatial dimensions and one spectral dimension ($x \times y \times z \times \upsilon$). For the complex spectrum, υ, spectral ghosting was corrected at each point (x,y,z),[43] an improved estimate of the frequency of the water peak was determined,[44] and real and imaginary components were phased to produce pure absorption and dispersion spectra. Spectra were phased using conventional techniques. Spectra were initially corrected based on the phase of the first echo. Subsequently, phase was changed iteratively until the integral under the absorption spectrum was maximized. Because models of water spectra from white matter[22–24] indicate that the frequency shifts between compartments is on the order of tens of Hz, a spectral bandwidth of 111 Hz was considered sufficient to resolve the water resonance. Additionally, at 9.4 T fat is ~1380 Hz from water (3.5 ppm). This chemical shift would result in the fat resonance aliasing ~12.43 times. After 12 complete aliases of the peak, an additional partial alias of 0.43 would place a fat peak approximately 47 Hz from water. This is almost exactly half the spectral bandwidth, ensuring that the fat resonance did not alias onto the water resonance.

B_0 maps were constructed from 3D-HiSS datasets. Because of the voxel-by-voxel improved estimation of the peak location[44] in the spectral processing described above, B_0 maps were produced with greater precision than the nominal spectral resolution of the raw data.

Water peak height images were constructed with signal intensity equal to the maximum signal intensity of the water spectrum in each voxel.[45] Fourier component images (FCIs) were constructed after shifting the peak of the water resonance in each voxel to the central spectral bin (υ_0). If we consider a specific frequency offset (for example, −3.5 Hz) from the water peak, υ_0, the FCI at spectral position $\upsilon_{-3.5}$ would have a signal variation that is dependent on the pixel-by-pixel signal intensity at −3.5 Hz from the peak of the water resonance. Note that because the peak of the water spectrum is always shifted to the central bin, information inherent in local shifts in B_0 is lost. In the future, efforts will be made to reliably correct for macroscopic variations in B_0, while retaining local shifts that reflect local magnetic susceptibility.

3. RESULTS

3.A. Water peak height images

Figure 2(a) shows a typical sagittally oriented water peak height image from a 3D EPSI acquisition. The white matter is clearly delineated, providing a distinct outline of the fornix. Other features, such as the layers in the olfactory bulb and cortical layers are also visible. Of particular interest is the cerebellum, due to the evident cytoarchitecture [Fig. 2(b)]. The Purkinje cell layer (PCL) is fully resolved[46] in all of Culmen lobule IV and V (4 and 5 Cb), Culmen lobule IV (6 Cb), and partially resolved elsewhere. Further, many of the fissures are also fully resolved (preculminate fissure and primary fissure) or partially resolved (precentral fissure, posterior superior fissure, prepyramidal fissure, secondary fissure, and posterolateral fissure). The molecular and granular layers are visible throughout all lobules of the cerebellum. However, they are not always clearly distinguished from one another due to variable contrast in the Purkinje layer. These features correlate with Giemsa + retinal projections stained histology [Fig. 2(d)].[47] These features of the cerebellum are less visible in the T_2^*-weighted image [Fig. 2(c)] produced from the fifth echo of the EPSI echo-train (TE = 50.37 ms).

Figure 3(a) shows a typical coronally oriented water peak height image from a 3D EPSI acquisition. Delineation of the corpus callosum from adjacent white matter tracts (e.g., dorsal hippocampal commissure) as well as cortical layers and the hippocampus are easily identified. Figure 3(b) shows typical results in the anterior portion of the hippocampal formation. The structures visible in these water peak height images are consistent with anatomy previously demonstrated by MR imaging using an exogenous contrast agent introduced during the fixative process.[48–52] Of interest, the pyramidal layer appears multilaminar,[53–56] a feature that correlates with acetylcholinesterase staining [Fig. 3(c)].[47] As noted by Slomianka *et al.*,[55,56] since acetylcholinesterase staining is

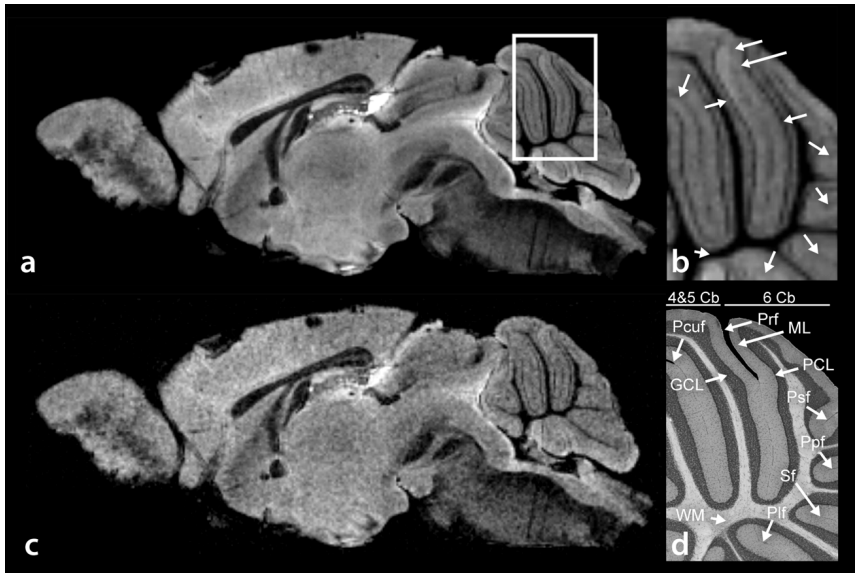

FIG. 2. (a) Sagittal water peak height image of mouse brain. (b) Magnified water peak height image of the cerebellum as defined by the white square in (a). The arbor vitae, granular cell layer, Purkinje cell layer, and molecular cell layer are clearly resolved, as corroborated by histology. (c) T_2^*-weighted image. (d) Histological identification of Culmen lobules IV and V (4 and 5 Cb), Culmen lobule 6 (6 Cb), primary fissure (Prf), molecular layer (ML), Purkinje cell layer (PCL), posterior superior fissure (Psf), prepyramidal fissure (Ppf), secondary fissure (Sf), posterolateral fissure (Plf), white matter (WM), granular cell layer (GCL), and the preculminate fissure (Pcuf).

depleted in the pyramidal cell bodies, the most compacted cell body areas of the layer showed less staining, giving the pyramidal layer a multilaminar appearance. Similarly, the most compacted cell body part of the pyramidal layer appears bright in the water peak height image [Fig. 3(b)]. Note, however, that the bright band of the pyramidal layer is not fully resolved over its entire length.

3.B. B_0 maps

Use of "FASTMAP" produced a very high degree of field homogeneity. Using a linear fit to approximate the average macroscopic gradient, the variations in B_0 were 6.16 ± 1.02, 3.01 ± 0.61, and $1.94 \pm 2.26(\times 10^{-3})$ G/cm in the x, y, and z directions (as per the B_0 coordinate system), respectively. Figure 4(b) shows a typical B_0 map through a coronal cross section of the hippocampus [Fig. 4(a)]. For reference, the main magnetic field direction was perpendicular to that of the image plane. With appropriate window and level adjustments of the B_0 map in Fig. 3(b), many of the individual layers of the hippocampus become clearly visible [Fig. 4(c)], including the pyramidal cell layer, the lacunosum molecular layer, and the granular layer of the dendate gyrus. This indicates that anatomic or physiologic differences between various layers of the hippocampus produce different bulk magnetic susceptibilities, and thus measureable local changes in B_0. While varying degrees of myelination may contribute to this in the hippocampus, other possible factors include cellular density, orientation, and cell size. For example, both the dendate gyrus and the pyramidal layer are composed of

FIG. 3. (a) Coronal water peak height image of mouse brain. (b) Magnified water peak height image of one half of the hippocampus as defined by the white square in (a). Arrows indicate the following features: molecular layer (Mol), stratum lacunosum-moleculare (Lmol), stratum oriens (Or), pyramidal layer (Py), stratum radiatum (Rad), granular layer of dentate gyrus (GrDG), and polymorph layer of dentate gyrus (PoDG). Arrows in (c), which is acetylcholinesterase staining of the hippocampus, correlate with arrows in (b).

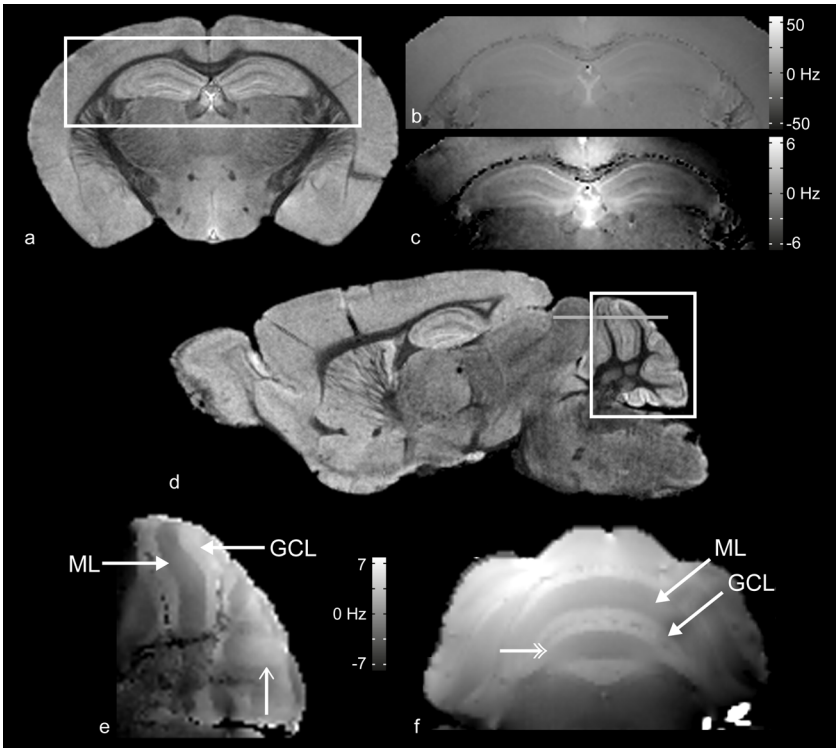

FIG. 4. (a) Coronal water peak height image of mouse brain. (b) B_0 map of the region of the hippocampus defined by the white square in (a). The image is windowed so as to cover the entire range of peak location values (±56 Hz), demonstrating the uniformity of the shimming over the region displayed. If the windowing is narrowed to a very small range (±7 Hz), as seen in (c), the anatomic details of the hippocampus become increasingly more distinctly resolved. (d) Sagittal water peak height image of mouse brain. (e) B_0 map of the region of the cerebellum defined by the white square in (d). The granular cell (GCL) and molecular (ML) layers induce different shifts in resonance frequency and are visually distinct from one another. (f) B_0 map of the region of the cerebellum defined by the gray horizontal line in (d).

differently sized cell bodies and cellular densities and also produce different field shifts.

Figure 4(e) demonstrates a typical sagittal B_0 map through the cerebellum [Fig. 4(d)]. The main magnetic field was oriented parallel to the image plane. A 6.76 ± 0.55 Hz shift (approximately 0.017 ppm) was detected between the molecular and granular layers of lobules IV and V of the Culmen.[46] The magnitudes of these shifts depend on orientation with respect to the main magnetic field and, therefore, reproducible positioning is critical for these measurements.

Typical unshifted phased absorption spectra, from which a B_0 map of the cerebellum similar to Fig. 4(e) was produced, are shown in Fig. 5(a). All spectra in the first two columns represent voxels from the molecular layer; the center two columns, the Purkinje cell layer; and the final two columns, the granular layer. The peak locations in all molecular layer spectra are shifted −7 Hz from those in the granular layer, which is consistent with the measured frequency shift from the B_0 map previously reported. The peak height in these voxels decreases as they approach the phase interface between the molecular layer and the granular layer. Further, the water line visibly broadens due to a shoulder/secondary peak that becomes resolved at +7 Hz above the frequency of the molecular layer. As voxels begin to have a greater volume fraction in the granular layer, the new peak at +7 Hz from the peak location in the molecular layer increases in height, the lower frequency peak decreases, eventually disappearing, and the new peak becomes the sole tall narrow peak. This clearly demonstrates that frequency dependent shoulders and secondary peaks reflect underlying anatomy, in this case, interfaces between two different tissues.

3.C. Fourier component images

Figure 6 shows a typical series of FCIs of the medial portion of the sagittal brain. Of the features visible in the water peak height image [Fig. 6(d)], the white matter fiber tract bundles appear with the lowest signal intensities, including the corpus callosum, the columns of the fornix, the ventral hippocampal commissure, the stria medularis, and the anterior commissure of the olfactory lobe. However, as seen in FCIs in Fig. 6(b), these features have higher relative signal intensities at −7.0 Hz compared with the surrounding tissue. This indicates an asymmetric shoulder of the water resonance along the low frequency side of the water resonance (relative to the peak), which is most clearly resolved at −7 Hz and is associated with the presence of myelinated white matter fiber tracts. The mottled appearance of FCIs at increasing and decreasing frequencies from that of the main water peak reflects the decreased signal-to-noise ratio associated with increasingly larger frequency shifts. To partially compensate for this, each FCI in Fig. 6 is individually windowed to improve the relative contrast. FCIs beyond ±10.5 Hz have insufficient signal-to-noise ratio to be useful.

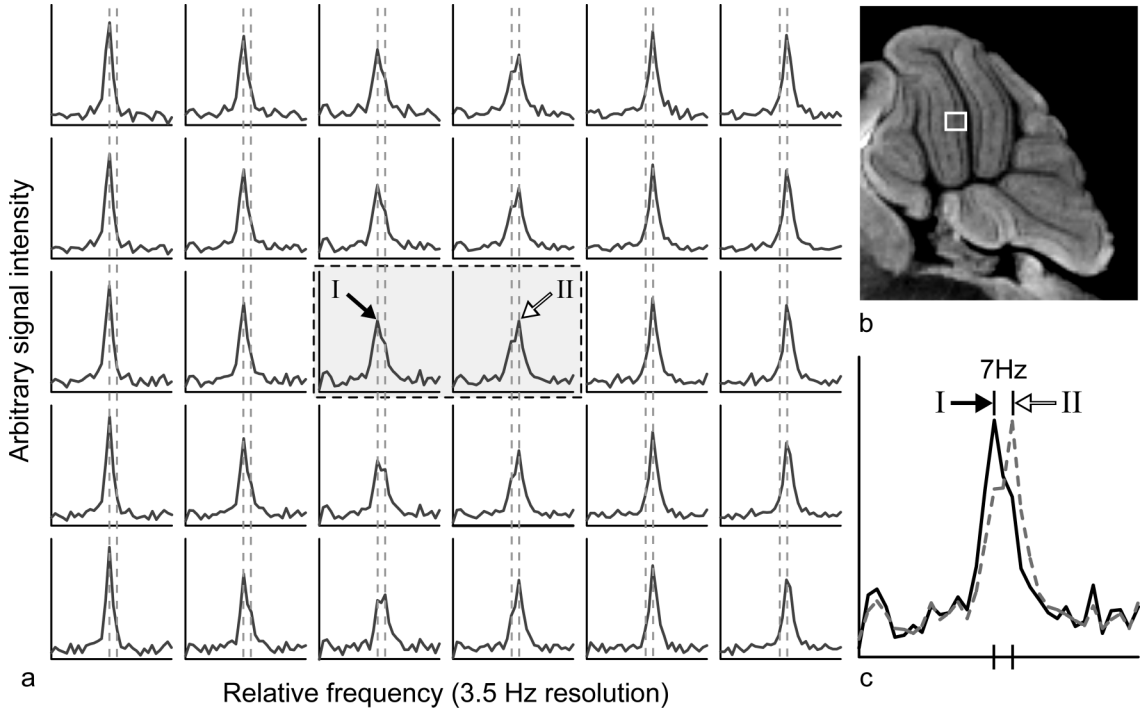

FIG. 5. (a) A matrix of contiguous spectra indicated by the white box in (b) the PH image of the cerebellum. The box indicates (from L to R) the molecular, Purkinje cell, and granular layers. (c) The spectra from (a) in the center that are inside the dashed line box. These are overlain to demonstrate the 7 Hz frequency shift between the main water peaks of the two spectra. Numerals I and II indicate the respective peaks in the array of spectra. The peaks in all voxels of the left three columns are shift 7 Hz from those in the right three columns (the two vertical dashed lines indicate this shift).

As previously described, the Purkinje cell layer is clearly visible in the water peak height image [Fig. 2(b)]. The Purkinje layer is also visible in the FCI at 7 Hz above the water peak frequency. The plot in Fig. 7(c) demonstrates that where there is a decrease in signal in the water peak height image at the Purkinje layer due to a shift of a component of the water signal, there is a relative increase in signal at 7 Hz. As with the aforementioned white matter tracts in the sagittal brain (Fig. 6), the Fourier components are not symmetric about the peak, i.e., the Purkinje layer is not visible at −7 Hz from the main water peak. This demonstrates that there is an asymmetric change of the water resonance at the Purkinje layer, on the high frequency side (relative to the water peak). This spectral feature is most clearly resolved at 7 Hz and distinguishes the Purkinje layer from surrounding tissue.

4. DISCUSSION

The water peak height images produced from high spectral and spatial resolution MRI allow identification of many layers and structures in the brain. Specifically, individual layers of the cerebellum and hippocampus that can be identified with various histological and/or acetylcholinesterase staining have been resolved. Many of these features have been identified using other MRI methods, *in vivo* and *ex vivo*, as well as with and without contrast agents.[57–62] However, the high spectral resolution of the data acquired here provides additional information. For example, the water peak height images show apparent sublayers of both the pyramidal cell and stratum radiatum of the hippocampus that are visible in histochemical staining using acetylcholinesterase.[55,56] This

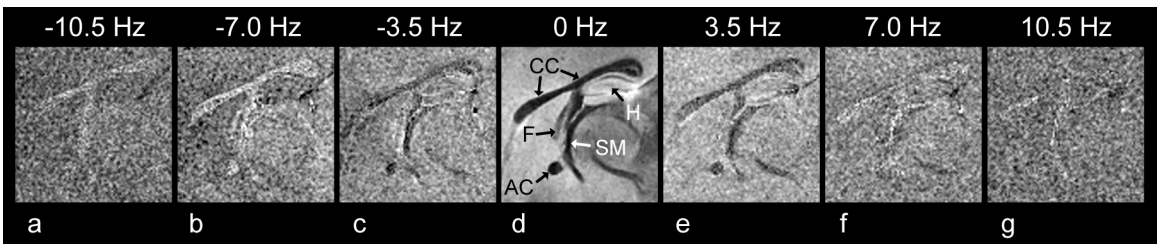

FIG. 6. A series of sagittally oriented FCIs (from −10.5 to 10.5 Hz, including the water peak height image at 0 Hz) showing the corpus callosum and other white matter fiber tracts. (d) The following features are identified in the water peak height image (0 Hz): Hippocampus (H), corpus callosum (CC), fornix (F), anterior commissure (AC), and stria medullaris (SM). The number at the top of each individual panel indicates the frequency of the particular FCI from the water peak height image. The white matter tracts demonstrate the presence of a consistent secondary peak/shoulder in the waterline at −7.0 Hz, as seen by the reversal in contrast relative to the surrounding tissue compared with that of the water peak height image. This effect is not seen as clearly at frequencies above that of the water peak.

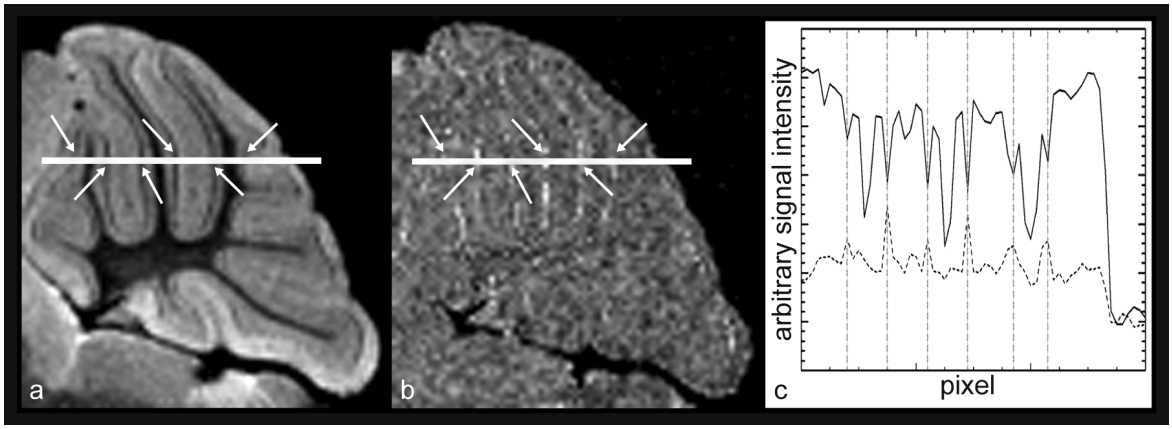

FIG. 7. (a) Water peak height image of the mouse cerebellum. (b) FCI at 7.0 Hz above the water peak. A reversal in image contrast is visible in the Purkinje cell layer where the signal intensity is greater than the surrounding layers of the cerebellum. This feature is not seen at −7.0 Hz. In the water peak height image, the Purkinje cell layer appears dark relative to the surrounding layers. (c) A plot of the signal intensity across the white line shown in figures (a) and (b) [solid and dashed line in (c), respectively]. The arrows in (a) and (b) identify the same positions as the vertical dashed lines in (c), which indicate the Purkinje cell layer. At each point that the Purkinje cell layer is crossed, the water peak height image shows a decrease in signal intensity, whereas the FCI shows an increase.

indicates that the water resonance peak height is sensitive to subtle underlying microstructural heterogeneity in what typically appears on MRI as a more homogenous feature. Moreover, this multilaminar appearance in the water peak height image does not have the same appearance in the B_0 image. This suggests that there are subtle local anatomic and/or physiologic variations that affect water resonance lineshape, T_2^*, and water resonance peak height without producing detectable changes in the measured resonance frequency of the bulk water over each voxel.

Water peak height images provide strong T_2^* contrast without the low SNR that is typical of conventional heavily T_2^*-weighted gradient echo images. The peak amplitude of the waterline is particularly sensitive to subtle, local variations in magnetic field strength. Small localized changes in bulk magnetic susceptibility can change both the T_2^* and resonance frequency in subvoxel environments, which in turn affects the magnitude of the peak height and produces very detailed images. Another example of this is the clear difference in contrast between white matter in both the corpus callosum and the arbor vitae of the cerebellum with that of the surrounding cortical tissue. Previously published work suggests that this is, at least in part, due to microscopic susceptibility effects in white matter associated with large concentrations of myelin.[63]

The effects of bulk magnetic susceptibility on resonance frequency and other characteristics of the water resonance are often dependent on orientation relative to B_0. Lee *et al.*[64] demonstrated that rotating parallel white matter nerve bundles 90° relative to the direction of the main magnetic field produced a measureable shift in resonance frequency. A similar effect is demonstrated in the B_0 map of the cerebellum in Fig. 4(e). A clear difference is visible between the molecular and granular layers, as indicated by the frequency shift between them. This shift is greatest in areas where the layers run parallel to B_0 and is reduced in areas where the fibers run perpendicular. The fibers of the granule cells tend to lie parallel to B_0 as they pass through the granular layer to the molecular layer. Once they have reached the molecular layer, the axons of the granule cells bend 90°, and then travel perpendicular to B_0.[65] These anisotropic structural components of each layer may be sufficient to affect the local resonance frequency. This suggests that the local B_0 field reflects underlying architecture and complements the anatomic information from water peak height images, which is consistent with previously published studies performed using T_2^*-weighted images, phase sensitive images, and susceptibility weighted imaging (SWI).[14–21] Interestingly, Figs. 4(e) and 4(f) show a relative frequency inversion and frequency convergence between the labeled layers, respectively (the unlabeled single and double headed line arrows), that corresponds to a change in orientation of the axons in the granular cell layer; specifically, the axons become oriented perpendicular to B_0. This is consistent with a geometric dependence of local bulk magnetic susceptibility relative to the main magnetic field.[66]

Differences in contrast between the peak height image and specific FCIs, such as those demonstrated in the white matter tracts and the Purkinje cell layer in Fig. 7, are a promising source of anatomic and/or cytoarchitectural information. These contrast differences in FCIs are due to asymmetric broadening of the water resonance because of either wholly or partially resolved secondary peaks to either side of the main water peak. Contrast in FCIs is related to the contrast in water peak height images, T_2^*-weighted images, and phase sensitive images, since variations in the amplitudes of off-peak Fourier components directly affect the water peak height and T_2^*, as well as the resonance frequency of the peak of the water resonance. However, FCIs may provide a more quantitative, specific, and sensitive method for isolating distinct components of the water resonance that are associated with subvoxel structures. Both theory and experimental evidence indicate that such non-Lorentzian spectral features are due to small (perhaps microscopic) compartments with differing magnetic susceptibility within a voxel.[32,45,67–70]

Spees *et al.*[71] demonstrate the effects on the water resonance due to settling erythrocytes in a blood sample using

measurements of the FID. Their results clearly demonstrate that as the two mixed compartments in the blood sample separate from one another, two distinct Fourier components form, each with slightly differing, resolvable resonances. The prevalence of analogous features in this work suggests that different compartments within each voxel are characterized by a different resonance frequency, T_2^*, as well as other MRI parameters. These compartments may be resolvable using high spectral and spatial resolution imaging, which is demonstrated in the spectra shown in Fig. 5(a). Moreover, the layer-dependent B_0 field change in the cerebellum is clearly shown in the spectra. The water resonance frequency changes near the interface between the molecular and the granular layers of the cerebellum. In voxels that include the interface, and therefore contain both layers, the main peak intensity decreases and a secondary peak becomes visible. FCIs have the potential to clearly show these two distinct components of the water resonance and thus delineate the boundary between two different types of tissue.

The spectral dimension has potential to increase the effective spatial resolution by resolving compartments that may be much smaller than the size of the voxel, or anatomic/physiologic features that are heterogeneously distributed within a voxel. Once the compartments are resolved in the spectral domain, it is possible that other properties of each compartment could be measured to provide additional information (e.g., the T_1, T_2, and apparent diffusion coefficient of each partially resolved component of the water resonance could be measured). This would contribute information regarding anatomic identification and/or cytoarchitecture. FCI's, high resolution B_0 maps, and other spectral features may provide anatomical information that complements diffusion tensor imaging, thereby assisting with imaging white matter tracts and other structural features as well.

The data presented here compliment previous studies using gradient echo imaging, phase-sensitive imaging, and SWI by providing detailed information concerning variations in water resonance frequency and lineshape. However, improvements in HiSS images are needed so that they can be more directly compared to images acquired using these other methods. While the images discussed here were acquired at very high resolution, they are not at the resolution that other investigators have reported.[72] In order to improve upon current results, it will be necessary to improve signal-to-noise ratio. This can be accomplished with higher field strength, higher gradient strength, smaller gradient set diameter, an improved detector (such as cryogenically cooled or phased array), and further improvements to shimming and data filtering. The gains in SNR that would come from these improvements would also decrease scan time, which would facilitate 3D-HiSS of *in vivo* brain.

Even without improvements in imaging speed and resolution, the data presented here demonstrate that HiSS imaging can accurately measure subtle variations in water resonance frequency and lineshape that resolve subtle features of brain anatomy. Since these variations produce contrast in T_2^*-weighted images, phase sensitive images, and SWI images, this quantitative information from HiSS can aid the interpretation of the results obtained using these faster and more commonly used methods.

5. CONCLUSION

Quantitative measurements with HiSS MRI allow quantitative and sensitive measurements of the variations in water resonance frequency and lineshape that produce contrast in T_2^*- weighted imaging, phase-sensitive, and susceptibility-weighted imaging. Therefore, HiSS MRI can provide information that complements and aids interpretation of images produced with more commonly used, faster imaging methods. In addition, FCIs produced from HiSS data may increase sensitivity to microscopic compartments with different magnetic susceptibilities. Although the images shown here were acquired *ex vivo* with very long run-times, with improved sampling methods and scanner sensitivity, similar images could be acquired with reasonable run times *in vivo*.

ACKNOWLEDGMENTS

This study was supported by U.S. Public Health Service Grant Nos. PO1 HD-009402 (N.B.S.) and P30 HD-054275 (N.B.S.) (ARRA supplement). S.F. would also like to thank Jennifer Neely for editing and proofreading.

NOMENCLATURE

HiSS	High spectral and spatial resolution
EPSI	Echo-planar spectroscopic imaging
FID	Free induction decay
PBS	Phosphate buffer saline solution
FOV	Field of view
NEX	Number of excitations
FCI	Fourier component image
SWI	Susceptibility weighted imaging

[a]Author to whom correspondence should be addressed. Electronic mail: sean.foxley@ndcn.ox.ac.uk; Telephone: +44 (0)1865 222 488; Fax: +44 (0)1865 222 717. Present address: FMRIB Centre, University of Oxford, Nuffield Department of Clinical Neurosciences, John Radcliffe Hospital, Headington, Oxford OX3 9DU, United Kingdom.

[1]Y. Jiang and G. A. Johnson, "Microscopic diffusion tensor imaging of the mouse brain," NeuroImage **50**, 465–471 (2010).

[2]R. M. Henkelman, L. Baghdadi, and J. G. Sled, "Presentation of 3D isotropic imaging data for optimal viewing," Magn. Reson. Med. **56**, 1371–1374 (2006).

[3]G. A. Johnson, A. Ali-Sharief, A. Badea, J. Brandenburg, G. Cofer, B. Fubara, S. Gewalt, L. W. Hedlund, and L. Upchurch, "High-throughput morphologic phenotyping of the mouse brain with magnetic resonance histology," NeuroImage **37**, 82–89 (2007).

[4]G. A. Johnson, G. P. Cofer, S. L. Gewalt, and L. W. Hedlund, "Morphologic phenotyping with MR microscopy: The visible mouse," Radiology **222**, 789–793 (2002).

[5]N. Kovacevic, J. T. Henderson, E. Chan, N. Lifshitz, J. Bishop, A. C. Evans, R. M. Henkelman, and X. J. Chen, "A three-dimensional MRI atlas of the mouse brain with estimates of the average and variability," Cereb. Cortex **15**, 639–645 (2005).

[6]J. P. Lerch, J. B. Carroll, A. Dorr, S. Spring, A. C. Evans, M. R. Hayden, J. G. Sled, and R. M. Henkelman, "Cortical thickness measured from MRI in the

YAC128 mouse model of Huntington's disease," NeuroImage **41**, 243–251 (2008).
[7]N. Chuang, S. Mori, A. Yamamoto, H. Jiang, X. Ye, X. Xu, L. J. Richards, J. Nathans, M. I. Miller, A. W. Toga, R. L. Sidman, and J. Zhang, "An MRI-based atlas and database of the developing mouse brain," NeuroImage **54**, 80–89 (2011).
[8]X. He and D. A. Yablonskiy, "Biophysical mechanisms of phase contrast in gradient echo MRI," Proc. Natl. Acad. Sci. U. S. A. **106**, 13558–13563 (2009).
[9]J. J. M. Zwanenburg, M. J. Versluis, P. R. Luijten, and N. Petridou, "Fast high resolution whole brain T2* weighted imaging using echo planar imaging at 7T," NeuroImage **56**, 1902–1907 (2011).
[10]G. Bartzokis, J. Cummings, S. Perlman, D. B. Hance, and J. Mintz, "Increased basal ganglia iron levels in Huntington disease," Arch. Neurol. **56**, 569–574 (1999).
[11]G. Bartzokis, J. L. Cummings, C. H. Markham, P. Z. Marmarelis, L. J. Treciokas, T. A. Tishler, S. R. Marder, and J. Mintz, "MRI evaluation of brain iron in earlier- and later-onset Parkinson's disease and normal subjects," Magn. Reson. Imaging **17**, 213–222 (1999).
[12]C. Mainero, T. Benner, A. Radding, A. van der Kouwe, R. Jensen, B. R. Rosen, and R. P. Kinkel, "In vivo imaging of cortical pathology in multiple sclerosis using ultra-high field MRI," Neurology **73**, 941–948 (2009).
[13]J. Stankiewicz, S. S. Panter, M. Neema, A. Arora, C. E. Batt, and R. Bakshi, "Iron in chronic brain disorders: Imaging and neurotherapeutic implications," Neurotherapeutics **4**, 371–386 (2007).
[14]J. Lee, M. Fukunaga, and J. H. Duyn, "Improving contrast to noise ratio of resonance frequency contrast images (phase images) using balanced steady-state free precession," NeuroImage **54**, 2779–2788 (2011).
[15]J. H. Duyn, P. van Gelderen, T.-Q. Li, J. A. de Zwart, A. P. Koretsky, and M. Fukunaga, "High-field MRI of brain cortical substructure based on signal phase," Proc. Natl. Acad. Sci. U. S. A. **104**, 11796–11801 (2007).
[16]E. M. Haacke, Y. Xu, Y.-C. N. Cheng, and J. R. Reichenbach, "Susceptibility weighted imaging (SWI)," Magn. Reson. Med. **52**, 612–618 (2004).
[17]R. M. Lebel, A. Eissa, P. Seres, G. Blevins, and A. H. Wilman, "Quantitative high-field imaging of sub-cortical gray matter in multiple sclerosis," Mult. Scler. **18**, 433–441 (2012).
[18]W. Li, B. Wu, A. V. Avram, and C. Liu, "Magnetic susceptibility anisotropy of human brain in vivo and its molecular underpinnings," NeuroImage **59**, 2088–2097 (2012).
[19]A. Rauscher, J. Sedlacik, M. Barth, E. M. Haacke, and J. R. Reichenbach, "Nonnvasive assessment of vascular architecture and function during modulated blood oxygenation using susceptibility weighted magnetic resonance imaging," Magn. Reson. Med. **54**, 87–95 (2005).
[20]P. Sipila, S. Greding, G. Wachutka, and F. Wiesinger, "2H transmit-receive NMR probes for magnetic field monitoring in MRI," Magn. Reson. Med. **65**, 1498–1506 (2011).
[21]E. Yamashita, Y. Kanasaki, S. Fujii, T. Tanaka, Y. Hirata, and T. Ogawa, "Comparison of increased venous contrast in ischemic stroke using phase-sensitive MR imaging with perfusion changes on flow-sensitive alternating inversion recovery at 3 Tesla," Acta Radiol. **52**, 905–910 (2011).
[22]W. C. Chen, S. Foxley, and K. L. Miller, "Detecting microstructural properties of white matter based on compartmentalization of magnetic susceptibility," NeuroImage **70**, 1–9 (2013).
[23]P. Sati, P. van Gelderen, A. C. Silva, D. S. Reich, H. Merkle, J. A. de Zwart, and J. H. Duyn, "Micro-compartment specific T2* relaxation in the brain," NeuroImage **77**, 268–278 (2013).
[24]S. Wharton and R. Bowtell, "Fiber orientation-dependent white matter contrast in gradient echo MRI," Proc. Natl. Acad. Sci. U. S. A. **109**, 18559–18564 (2012).
[25]M. Doyle and P. Mansfield, "Chemical-shift imaging: A hybrid approach," Magn. Reson. Med. **5**, 255–261 (1987).
[26]P. Mansfield, "Spatial mapping of the chemical shift in NMR," Magn. Reson. Med. **1**, 370–386 (1984).
[27]Y. P. Du, R. Chu, D. Hwang, M. S. Brown, B. K. Kleinschmidt-DeMasters, D. Singel, and J. H. Simon, "Fast multislice mapping of the myelin water fraction using multicompartment analysis of T2* decay at 3T: A preliminary postmortem study," Magn. Reson. Med. **58**, 865–870 (2007).
[28]X. Fan, H. Abe, M. Medved, S. Foxley, S. Arkani, M. A. Zamora, O. I. Olopade, G. M. Newstead, and G. S. Karczmar, "Fat suppression with spectrally selective inversion vs. High spectral and spatial resolution MRI of breast lesions: Qualitative and quantitative comparisons," J. Magn. Reson. Imaging **24**, 1311–1315 (2006).
[29]M. Medved, X. Fan, H. Abe, G. M. Newstead, A. M. Wood, A. Shimauchi, K. Kulkarni, M. K. Ivancevic, L. L. Pesce, O. I. Olopade, and G. S. Karczmar, "Non-contrast enhanced MRI for evaluation of breast lesions: Comparison of non-contrast enhanced high spectral and spatial resolution (HiSS) images versus contrast enhanced fat-suppressed images," Acad. Radiol. **18**, 1467–1474 (2011).
[30]M. Medved, G. M. Newstead, H. Abe, O. I. Olopade, A. Shimauchi, M. A. Zamora, and G. S. Karczmar, "Clinical implementation of a multislice high spectral and spatial resolution-based MRI sequence to achieve unilateral full-breast coverage," Magn. Reson. Imaging **28**, 16–21 (2010).
[31]W. Du, X. Fan, S. Foxley, M. Zamora, J. N. River, R. M. Culp, and G. S. Karczmar, "Comparison of high-resolution echo-planar spectroscopic imaging with conventional MR imaging of prostate tumors in mice," NMR Biomed. **18**, 285–292 (2005).
[32]S. Foxley, X. Fan, S. A. Jansen, M. Zamora, E. Markiewicz, H. Al-Ahmadie, and G. S. Karczmar, "High spectral and spatial resolution MRI of age-related changes in murine prostate," Magn. Reson. Med. **60**, 575–581 (2008).
[33]C. R. Haney, C. A. Pelizzari, S. Foxley, M. A. Zamora, D. Mustafi, M. Tretiakova, S. Li, X. Fan, and G. S. Karczmar, "HiSStology: High spectral and spatial resolution magnetic resonance imaging detection of vasculature validated by histology and micro-computed tomography," Mol. Imaging **10**, 187–196 (2011).
[34]W. Du, G. S. Karczmar, S. J. Uftring, and Y. P. Du, "Anatomical and functional brain imaging using high-resolution echo-planar spectroscopic imaging at 1.5 Tesla," NMR Biomed. **18**, 235–241 (2005).
[35]R. C. Mandl, M. P. van den Heuvel, D. W. Klomp, V. O. Boer, J. C. Siero, P. R. Luijten, and H. E. Hulshoff Pol, "Tract-based magnetic resonance spectroscopy of the cingulum bundles at 7 T," Hum. Brain Mapp. **33**, 1503–1511 (2012).
[36]S. Posse, Z. Shen, V. Kiselev, and L. J. Kemna, "Single-shot T(2)* mapping with 3D compensation of local susceptibility gradients in multiple regions," NeuroImage **18**, 390–400 (2003).
[37]S. Sarkar, K. Heberlein, G. J. Metzger, X. Zhang, and X. Hu, "Applications of high-resolution echoplanar spectroscopic imaging for structural imaging," J. Magn. Reson. Imaging **10**, 1–7 (1999).
[38]R. Gruetter, "Automatic, localized in vivo adjustment of all first- and second-order shim coils," Magn. Reson. Med. **29**, 804–811 (1993).
[39]J. Budde, G. Shajan, J. Hoffmann, K. Ugurbil, and R. Pohmann, "Human imaging at 9.4 T using T(2) *-, phase-, and susceptibility-weighted contrast," Magn. Reson. Med. **65**, 544–550 (2011).
[40]C. Sergeant, M. H. Vesvres, G. Deves, and F. Guillou, "Calcium, potassium, iron, copper and zinc concentrations in the white and gray matter of the cerebellum and corpus callosum in brain of four genetic mouse strains," Nucl. Instrum. Methods Phys. Res., Sect. B **231**, 234–238 (2005).
[41]T. M. Shepherd, P. E. Thelwall, G. J. Stanisz, and S. J. Blackband, "Aldehyde fixative solutions alter the water relaxation and diffusion properties of nervous tissue," Magn. Reson. Med. **62**, 26–34 (2009).
[42]S. Foxley, X. Fan, J. River, M. Zamora, E. Markiewicz, S. Sokka, and G. S. Karczmar, "Hyperthermically induced changes in high spectral and spatial resolution MR images of tumor tissue–a pilot study," Phys. Med. Biol. **57**, 2653–2666 (2012).
[43]W. Du, Y. P. Du, X. Fan, M. A. Zamora, and G. S. Karczmar, "Reduction of spectral ghost artifacts in high-resolution echo-planar spectroscopic imaging of water and fat resonances," Magn. Reson. Med. **49**, 1113–1120 (2003).
[44]X. Fan, W. Du, P. MacEneaney, M. Zamora, and G. Karczmar, "Structure of the water resonance in small voxels in rat brain detected with high spectral and spatial resolution MRI," J. Magn. Reson. Imaging **16**, 547–552 (2002).
[45]H. A. Al-Hallaq, X. Fan, M. Zamora, J. N. River, J. E. Moulder, and G. S. Karczmar, "Spectrally inhomogeneous BOLD contrast changes detected in rodent tumors with high spectral and spatial resolution MRI," NMR Biomed. **15**, 28–36 (2002).
[46]K. Shmueli, J. A. de Zwart, P. van Gelderen, T.-Q. Li, S. J. Dodd, and J. H. Duyn, "Magnetic susceptibility mapping of brain tissue in vivo using MRI phase data," Magn. Reson. Med. **62**, 1510–1522 (2009).
[47]S. Mikula, I. Trotts, J. M. Stone, and E. G. Jones, "Internet-enabled high-resolution brain mapping and virtual microscopy," NeuroImage **35**, 9–15 (2007).
[48]G. A. Johnson, G. P. Cofer, B. Fubara, S. L. Gewalt, L. W. Hedlund, and R. R. Maronpot, "Magnetic resonance histology for morphologic phenotyping," J. Magn. Reson. Imaging **16**, 423–429 (2002).
[49]A. A. Sharief and G. A. Johnson, "Enhanced T2 contrast for MR histology of the mouse brain," Magn. Reson. Med. **56**, 717–725 (2006).

[50]X. Zhang, E. L. Bearer, A. T. Perles-Barbacaru, and R. E. Jacobs, "Increased anatomical detail by in vitro MR microscopy with a modified Golgi impregnation method," Magn. Reson. Med. **63**, 1391–1397 (2010).
[51]J. O. Cleary, F. K. Wiseman, F. C. Norris, A. N. Price, M. Choy, V. L. J. Tybulewicz, R. J. Ordidge, S. Brandner, E. M. C. Fisher, and M. F. Lythgoe, "Structural correlates of active-staining following magnetic resonance microscopy in the mouse brain," NeuroImage **56**, 974–983 (2011).
[52]J. O. Cleary, M. Modat, F. C. Norris, A. N. Price, S. A. Jayakody, J. P. Martinez-Barbera, N. D. E. Greene, D. J. Hawkes, R. J. Ordidge, P. J. Scambler, S. Ourselin, and M. F. Lythgoe, "Magnetic resonance virtual histology for embryos: 3D atlases for automated high-throughput phenotyping," NeuroImage **54**, 769–778 (2011).
[53]R. C. Green and M. M. Mesulam, "Acetylcholinesterase fiber staining in the human hippocampus and parahippocampal gyrus," J. Comp. Neurol. **273**, 488–499 (1988).
[54]V. K. Vijayan, "Distribution of cholinergic neurotransmitter enzymes in the hippocampus and the dentate gyrus of the adult and the developing mouse," Neuroscience **4**, 121–137 (1979).
[55]L. Slomianka and F. A. Geneser, "Distribution of acetylcholinesterase in the hippocampal region of the mouse: II. Subiculum and hippocampus," J. Comp. Neurol. **312**, 525–536 (1991).
[56]L. Slomianka and F. A. Geneser, "Distribution of acetylcholinesterase in the hippocampal region of the mouse: I. Entorhinal area, parasubiculum, retrosplenial area, and presubiculum," J. Comp. Neurol. **303**, 339–354 (1991).
[57]S. Boretius, L. Kasper, R. Tammer, T. Michaelis, and J. Frahm, "MRI of cellular layers in mouse brain in vivo," NeuroImage **47**, 1252–1260 (2009).
[58]T. Watanabe, J. Frahm, and T. Michaelis, "Cell layers and neuropil: Contrast-enhanced MRI of mouse brain in vivo," NMR Biomed. **26**, 1870–1878 (2013).
[59]O. Natt, T. Watanabe, S. Boretius, J. Frahm, and T. Michaelis, "Magnetization transfer MRI of mouse brain reveals areas of high neural density," Magn. Reson. Imaging **21**, 1113–1120 (2003).
[60]C. Baltes, N. Radzwill, S. Bosshard, D. Marek, and M. Rudin, "Micro MRI of the mouse brain using a novel 400 MHz cryogenic quadrature RF probe," NMR Biomed. **22**, 834–842 (2009).
[61]J. H. Lee, A. C. Silva, H. Merkle, and A. P. Koretsky, "Manganese-enhanced magnetic resonance imaging of mouse brain after systemic administration of MnCl2: Dose-dependent and temporal evolution of T1 contrast," Magn. Reson. Med. **53**, 640–648 (2005).
[62]M. Aggarwal, M. V. Jones, P. A. Calabresi, S. Mori, and J. Zhang, "Probing mouse brain microstructure using oscillating gradient diffusion MRI," Magn. Reson. Med. **67**, 98–109 (2012).
[63]T.-Q. Li, B. Yao, P. van Gelderen, H. Merkle, S. Dodd, L. Talagala, A. P. Koretsky, and J. Duyn, "Characterization of T(2)* heterogeneity in human brain white matter," Magn. Reson. Med. **62**, 1652–1657 (2009).
[64]J. Lee, K. Shmueli, M. Fukunaga, P. van Gelderen, H. Merkle, A. C. Silva, and J. H. Duyn, "Sensitivity of MRI resonance frequency to the orientation of brain tissue microstructure," Proc. Natl. Acad. Sci. U. S. A. **107**, 5130–5135 (2010).
[65]R. R. Llinas, K. D. Walton, and E. J. Lang, "Cerebellum," in *The Synaptic Organization of the Brain*, edited by G. M. Shepherd (Oxford University Press, NY, 2004).
[66]S. C. Chu, Y. Xu, J. A. Balschi, and C. S. Springer, Jr., "Bulk magnetic susceptibility shifts in NMR studies of compartmentalized samples: Use of paramagnetic reagents," Magn. Reson. Med. **13**, 239–262 (1990).
[67]S. Foxley, X. Fan, D. Mustafi, C. Haney, M. Zamora, E. Markiewicz, M. Medved, A. M. Wood, and G. S. Karczmar, "Sensitivity to tumor microvasculature without contrast agents in high spectral and spatial resolution MR images," Magn. Reson. Med. **61**, 291–298 (2009).
[68]S. Foxley, X. Fan, D. Mustafi, C. Yang, M. A. Zamora, M. Medved, and G. S. Karczmar, "Quantitative analysis of water proton spectral lineshape: A novel source of contrast in MRI," Phys. Med. Biol. **53**, 4509–4522 (2008).
[69]G. S. Karczmar, X. Fan, H. Al-Hallaq, J. N. River, K. Tarlo, K. E. Kellar, M. Zamora, C. Rinker-Schaeffer, and M. J. Lipton, "Functional and anatomic imaging of tumor vasculature: High-resolution MR spectroscopic imaging combined with a superparamagnetic contrast agent," Acad. Radiol. **9**(Suppl. 1), S115–S118 (2002).
[70]G. S. Karczmar, X. Fan, H. A. Al-Hallaq, M. Zamora, J. N. River, C. Rinker-Schaeffer, M. Zaucha, K. Tarlo, and K. Kellar, "Uptake of a superparamagnetic contrast agent imaged by MR with high spectral and spatial resolution," Magn. Reson. Med. **43**, 633–639 (2000).
[71]W. M. Spees, D. A. Yablonskiy, M. C. Oswood, and J. J. Ackerman, "Water proton MR properties of human blood at 1.5 tesla: Magnetic susceptibility, T(1), T(2), T*(2), and non-Lorentzian signal behavior," Magn. Reson. Med. **45**, 533–542 (2001).
[72]A. Badea, G. A. Johnson, and R. W. Williams, "Genetic dissection of the mouse CNS using magnetic resonance microscopy," Curr. Opin. Neurol. **22**, 379–386 (2009).